particles

Article

Beaming of Polarized Radiation in Subcritical X-Ray Pulsars

Ivan D. Markozov [1,2], Alexander Y. Potekhin [1,2,*], Alexander D. Kaminker [1] and Alexander A. Mushtukov [3,4]

[1] Ioffe Institute, Politekhnicheskaya 26, St. Petersburg 194021, Russia; markozoviv@mail.ru (I.D.M.); kam@astro.ioffe.ru (A.D.K.)
[2] Space Research Institute RAS, 84/32 Profsoyuznaya Street, Moscow 117997, Russia
[3] Mullard Space Science Laboratory, University College London, Holmbury St. Mary, Surrey RH5 6NT, UK; al.mushtukov@gmail.com
[4] Astrophysics, Department of Physics, University of Oxford, Denys Wilkinson Building, Keble Road, Oxford OX1 3RH, UK
* Correspondence: palex@astro.ioffe.ru

Abstract

Radiation of X-ray pulsars is powered by accretion on the neutron star surface from a binary companion under the influence of a strong magnetic field. We study the beaming of this radiation in the case of subcritical X-ray pulsars, where it is formed in the accretion channel close to the neutron star surface. We solve equations of the hydrodynamics and radiative transfer of two coupled polarization modes in the accretion channel numerically, taking into account resonant Compton scattering and vacuum polarization. The beaming patterns are obtained for different accretion rates, photon energies, and polarizations, as well as for different models of the neutron star surface radiation. The calculated beaming patterns are converted into light curves for both the intensity and polarization, taking into account the effects of General Relativity. These beaming patterns and light curves are found to be strongly affected by the resonant Compton scattering for photon energies comparable with the electron cyclotron energy. In particular, the angular redistribution of radiation near the cyclotron resonance may reduce the light-curve modulation amplitude, which is consistent with observational indications of a suppressed pulsed fraction at these energies.

Keywords: high energy astrophysical phenomena; radiative transfer; X-rays: binaries; stars: neutron; pulsars: general

1. Introduction

X-ray pulsars (XRPs) are strongly magnetized accreting neutron stars (NSs) in close binary systems (for a recent review, see [1]). In such systems, matter from the companion star falls onto the NS surface through an accretion channel along the field lines around magnetic poles. The kinetic energy of the accreting matter that hits the NS surface is mostly converted into X-ray radiation. Because of a misalignment of the magnetic and rotation axes of a NS, a remote observer detects a pulsating signal.

A typical field strength at the surface of an XRP is $B \sim 10^{12} - 10^{13}$ G. In such strong fields, the electron cyclotron energy

$$E_{\rm cyc} = \hbar\omega_{\rm cyc} = \frac{\hbar e B}{m_{\rm e} c} = 11.577\, B_{12}\ {\rm keV} \tag{1}$$

reaches tens keV, causing distinct quantum-mechanical effects. In Equation (1), $\hbar$ is the reduced Planck constant, c the speed of light, e the elementary charge, $m_{\rm e}$ the electron

Check for updates

Academic Editors: Aram Saharian and Armen Sedrakian

Received: 26 February 2026
Revised: 31 March 2026
Accepted: 9 April 2026
Published: 5 May 2026

Copyright: © 2026 by the authors. Licensee MDPI, Basel, Switzerland. This article is an open access article distributed under the terms and conditions of the Creative Commons Attribution (CC BY) license.

https://doi.org/10.3390/particles9020049

mass, $B_{12} \equiv B/10^{12}$ G and $\omega_{\rm cyc}$ is the electron cyclotron frequency. The mean free time of electrons is much larger than $\omega_{\rm cyc}^{-1}$ at typical plasma densities in the accretion channel, which effectively constrains the plasma motion to one dimension along $\boldsymbol{B}$.

Observed X-ray luminosities of the XRPs vary over several orders of magnitude, from $L_{\rm X} \lesssim 10^{33}$ to $L_{\rm X} \gtrsim 10^{41}$ erg s^{-1} [1,2] (with the reservation that the apparent super-Eddington luminosities of $L_{\rm X} \gtrsim 10^{38}$ erg s^{-1} in the ultraluminous sources [3,4] may be overestimated because of collimation [5–7], which is a hypothesis under debate – see, e.g., Ref. [8] and references therein). At low luminosities $L_{\rm X} \lesssim 10^{34}$ erg s^{-1}, the XRPs may undergo a slow accretion from a cold disk [9,10] or no accretion due to the propeller effect [11]. Cyclotron absorption lines have been observed in the spectra of nearly 40 XRPs, sometimes with one or a few harmonics [12]. Recently, due to the Imaging X-ray Polarimetry Explorer (IXPE) [13], it has become possible to measure the polarization of the X-ray radiation of the XRPs in the band of 2–8 keV (see, e.g., [14,15]).

The bolometric luminosity measured by a distant observer is related to the mass accretion rate $\dot{M}$ onto a NS with mass M and radius $R_{\rm NS}$ as [16,17]

$$L = \frac{z_{\rm g}\dot{M}c^2}{(1+z_{\rm g})^2} = 10^{36}\,\frac{1.327}{1+z_{\rm g}/2}\,\frac{M/M_\odot}{R_6}\,\dot{M}_{16}\ \mathrm{erg\ s^{-1}}, \tag{2}$$

where $z_{\rm g} = (1 - 2GM/c^2R_{\rm NS})^{-1/2} - 1$ is the gravitational redshift, G is the Newtonian constant of gravitation, $M_\odot$ the solar mass, $R_6 = R_{\rm NS}/10^6$ cm and $\dot{M}_{16} = \dot{M}/10^{16}$ g s^{-1}. Here $\dot{M}$ is measured in the local reference frame at the NS surface; the accretion rate measured by a remote observer is $\dot{M}^\infty = \dot{M}/(1+z_{\rm g})$. There is a critical value of luminosity ($L_{\rm crit} \sim 10^{36}$ erg s^{-1} for a typical XRP), at which radiation pressure can stop plasma motion [18]. XRPs with higher luminosities are called supercritical, while XRPs with lower luminosities are called subcritical. In the supercritical XRPs, a radiation-dominated shock is expected in the accretion channel [19]. The observed radiation of the supercritical XRPs originates from the accretion column, made of a slow-moving dense hot plasma below the shock front.

For the subcritical XRPs, two fundamentally different accretion regimes have been discussed. One of them is determined by Coulomb braking of the fast-moving plasma in a relatively thin layer near the NS surface [20]. This process leads to formation of heated atmosphere regions around the magnetic poles, from which the X-ray radiation emerges (e.g., [21]). In the other regime [22–24], a collisionless shock wave appears, which plays the crucial role in the accretion channel structure and radiation formation. In the present paper, we focus on the subcritical XRPs in the shockless regime.

In a previous work [25], we constructed a model of the accretion channel and calculated polarized radiation transfer in the electron-proton plasma approximation for the dielectric tensor. The model included the resonant scattering of radiation in a strong magnetic field, but neglected the damping of the electron cyclotron resonance, the ion cyclotron motion and vacuum polarization effects. Besides, we considered only the case of a completely filled accretion channel, which can probably be formed under the conditions of spherical accretion. A more realistic geometry of disc accretion favors the formation of a hollow channel, only partially filled with plasma [19]. A detailed study of the plasma hydrodynamics and polarized radiation transfer in the accretion channels of the subcritical XRPs with account of the vacuum polarization in both accretion channel geometries will be presented elsewhere [26]. Here, we focus on the influence of radiative transfer in the hollow accretion channel on the beaming of the outgoing radiation. As in the above-cited papers, the plasma is assumed to be composed of fully ionized hydrogen.

2. Physics Input and Numerical Methods

Propagation of electromagnetic waves in magnetized plasmas has been comprehensively described in the monograph by Ginzburg [27]. At circular frequencies ω, which lie sufficiently far from resonances and are much larger than the electron plasma frequency $\omega_{\mathrm{pe}} = \left(4\pi e^2 n_{\mathrm{e}}/m_{\mathrm{e}}\right)^{1/2}$, where n_{e} is the electron number density, radiation propagates in the form of two normal modes. The normal mode whose electric vector oscillates along an ellipse with a major axis lying in the plane formed by the photon wave vector $\boldsymbol{k}$ and magnetic field vector $\boldsymbol{B}$ is called ordinary (O-mode), and the normal mode whose polarization ellipse has a major axis perpendicular to this plane is called extraordinary (X-mode). The two modes have different absorption and scattering cross sections, which depend on the angle θ_B between $\boldsymbol{k}$ and $\boldsymbol{B}$, and interact with each other through scattering.

Gnedin and Pavlov [28] formulated the radiative transfer problem in terms of the normal modes and specified the applicability conditions of such description. They showed that in the conditions typical for strongly magnetized NSs, a strong Faraday depolarization occurs at most photon energies $E = \hbar\omega$ (except narrow frequency ranges near resonances), which allows one to consider specific intensities of the two normal modes instead of the four components of the Stokes vector.

The influence of the vacuum polarization on the NS radiation was first evaluated in [29,30] and studied in detail in subsequent works, summarized by Pavlov and Gnedin [31]. A further progress was made by Lai et al. [32–35], who used a more general formalism and studied the effect of normal mode conversion for radiation propagating in an inhomogeneous plasma across so-called vacuum resonance. At this resonance, the vacuum and plasma polarization effects become equally important, and the normal mode approximation is no longer valid. If the density variation is sufficiently gentle, the polarization of a photon evolves adiabatically, preserving the electric vector rotation direction, but changing the direction of the major axis of the rotation ellipse relative to the $\boldsymbol{k} - \boldsymbol{B}$ plane, which means the conversion between the O-mode and X-mode. This occurs at a plasma density $\rho_{\mathrm{vac}} \sim 10^{-4} B_{12}^2 (E/1\ \mathrm{keV})^2\ \mathrm{g\ cm}^{-3}$. Here, we follow the general formalism of Lai and Ho [34], but neglect the mode conversion, because the subcritical accretion channel is almost transparent to radiation at those relatively low photon energies, at which the plasma density ρ in the channel can reach ρ_{vac}. The non-trivial effects of Compton scattering in the accretion channel occur at higher E, where the X- and O-mode polarization vectors are almost linear, being determined mostly by the vacuum polarization effects.

Compton scattering in a strong magnetic field differs significantly from the field-free one. We treat it by analogy with our previous papers [25,36], but with certain improvements and corrections, as described in detail in [26]. We assume that an electron occupies the ground Landau level before and after scattering, which is generally a good approximation for the XRPs because of the quick radiative decay of the excited Landau states [37]. The differential cross sections of photon scattering on an electron in a strong magnetic field is adopted from Ref. [38], where it is given for an electron at rest and for the linear polarizations of the incoming and scattered photons. We transform the cross sections to the elliptical normal-mode polarization basis and average them over the relativistic thermal distribution of electron momenta parallel to $\boldsymbol{B}$ (the one-dimensional Maxwell–Jüttner distribution—see, e.g., Appendix A in Ref. [36]), using the Lorentz transformations of energies E and angles θ_B for the incoming and scattered photons of the cross sections. These cross sections are then employed in the numerical solutions of equations of radiation hydrodynamics for the one-dimensional plasma motion along the magnetic field lines and stationary radiative transfer equations for the two coupled normal modes. The stationary radiative transfer approximation is applicable because the typical time of photon propagation inside the accretion channel is short on the hydrodynamic time scale. In solving the system of radiation hydrodynamics equations, we assume that electrons and protons have the same temperature T and apply an ideal gas equation of state (EoS), which is a good approximation at the XRP conditions, because $T \sim$ a few keV is much higher than the hydrogen binding energy at $B \lesssim 10^{13}$ G. This plasma EoS is supplemented by the EoS of ideal photon gas, assuming the local thermodynamic equilibrium. However, as mentioned in Ref. [25], the exact EoS form is unimportant for our model calculations, because the accretion flow is mainly controlled by the gravity and radiation pressure, rather than by the EoS.

For a numerical solution of the problem, we use the time discretization and apply the operator splitting method [39]. Each time step is divided into three substeps.

At the first substep, we solve the hydrodynamical system of equations, neglecting the radiative terms. To solve this simplified system, we employ the open library VH-1 ('Virginia Hydrodynamics-1' [40]) (http://wonka.physics.ncsu.edu/pub/VH-1/ (accessed on 5 November 2022)). The numerical grid is organized as a hollow cylinder with an outer radius R_c, with inner radius $R_\mathrm{c} - d_\mathrm{w}$ (d_w being the thickness of the cylindrical walls) and height H, divided into a sufficient number of equal slices. We neglect variations in all hydrodynamic variables along the radius of the cylinder, because we have found previously [25] that these quantities do not significantly vary along the radial coordinate. The magnetic field and the cylinder axis are perpendicular to the NS surface. In the examples of calculations presented below, we have set $M = 1.4\,M_\odot$, $R_\mathrm{NS} = 12$ km. $R_\mathrm{c} = 0.5$ km and $d_\mathrm{w} = 15$ m. The height H is chosen sufficiently large to exceed the height of the zone where radiation pressure is significant, so that the plasma velocity at the upper face of the cylinder almost coincides with the free-fall velocity. Nevertheless $H \ll R_\mathrm{NS}$ in the subcritical regime [41]. The magnetic field strength $B = 4.319 \times 10^{12}$ G is chosen to provide the cyclotron energy $E_\mathrm{cyc} = 50$ keV, which is typical for the XRPs.

At the second substep, radiation transfer of the two coupled normal modes and the plasma-radiation energy-momentum exchange are simulated by the Monte Carlo method (see Ref. [36] for a detailed description of our Monte Carlo code). To accelerate these simulations, we use precalculated tables of the total scattering cross sections and cumulative distribution functions of probability of photon scattering into a given direction and given normal mode with initial E and θ_B. These tables are based on the differential cross sections and depend on ρ, T and E_cyc as parameters; their detailed description is given in Ref. [26].

At the third substep, the contribution of the radiative terms, which have been neglected at the first substep, is restored. The energy-momentum exchange between the electron-proton plasma and the photons is described by a system of first-order differential equations for time conservation of mass, energy, and momentum densities. These equations are solved by the explicit Euler method, which has been found appropriate in the case of subcritical pulsars.

We assume that the plasma is in the free-fall state at the top of the accretion channel and set its inflow velocity equal to the free-fall velocity $v_\mathrm{ff} = \sqrt{2GM/(R_\mathrm{NS} + H)} \approx \sqrt{2GM/R_\mathrm{NS}}$. The plasma density at the top boundary is determined by this velocity, the mass accretion rate $\dot{M}$ and the channel cross-section area $2\pi R_\mathrm{c} d_\mathrm{w}$, that is $\rho(H) = \dot{M}/2\pi R_\mathrm{c} d_\mathrm{w} v_\mathrm{ff}$.

The boundary conditions at the bottom of the channel are not so obvious. In our model, the bottom is placed at the NS surface. Therefore the proper bottom boundary conditions are determined by the physics of the interaction of the accreting plasma and radiation with the NS surface or the atmosphere, which is a complex, not completely solved problem. In the examples of simulations presented below, we assume that the total (plasma and radiation) energy that enters the NS surface is re-emitted by electromagnetic radiation with a specific intensity $I_E(\theta)$, where θ is an angle between the wave vector $\boldsymbol{k}$ and the NS surface normal. We assume that the surface radiation has the blackbody spectrum with a uniform temperature determined by the energy balance within the emitting ring, but we allow for possibly non-trivial initial polarization or beaming. For the polarization, we test the three extreme cases of non-polarized surface radiation (i.e., equal numbers of X- and O-photons of the same energy) and the radiation polarized entirely in either the X-mode or the O-mode. For the initial beaming, we apply the simplest non-isotropic model

$$I_E(\theta) \propto 1 + b\,\cos\theta, \tag{3}$$

where $b \geq -1$ is a free parameter. Then the radiant intensity (the energy per unit solid angle emitted by the hot spot of area S at the NS surface) $Q_E = S_\perp I_E(\theta) = S I_E(\theta)\cos\theta$, where $S_\perp = S\cos\theta$ is the projected transverse hot-spot area, follows the Lambert law $Q_E \propto \cos\theta$ at $b = 0$, while it is suppressed along the normal to the surface at $b < 0$ and more elongated at $b > 0$.

3. Results

3.1. General Features of Beaming

In the left panels of Figures 1–3 we present the calculated θ-dependencies of the radiation outgoing from the accretion channel at different photon energies. In the right panels, we show the corresponding beaming patterns in the polar coordinates. The surface radiation is assumed unpolarized. Each function $Q_E(\theta)$ is normalized to its maximum, in order to focus on the angular dependence. It should be noted that the parts of the curves with $\theta \geq 90°$ cannot be observed: since the radius and height of the accretion channel are small compared with the NS radius, the radiation that comes out at these angles goes back to the NS surface and contributes to its heating.

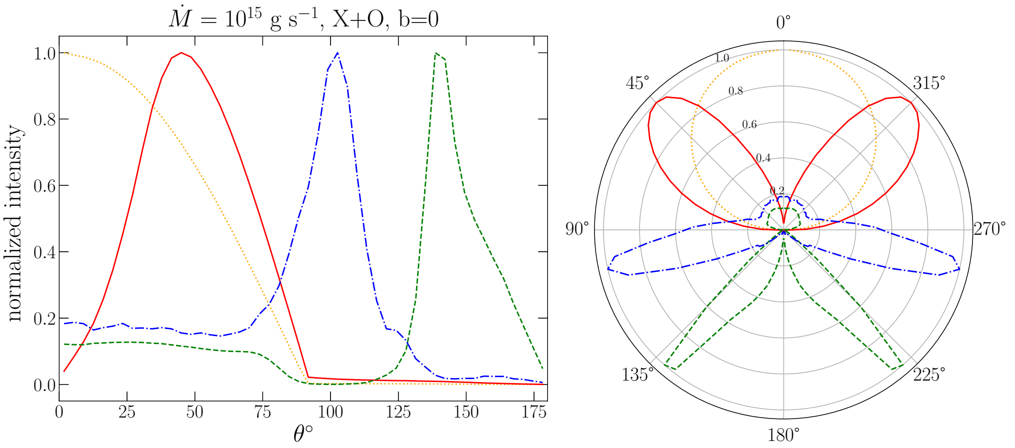

Figure 1. Dependence of the normalized radiant intensity Q_E on the polar angle θ (**left panel**) and corresponding beam pattern (**right panel**) at accretion rate $\dot{M} = 10^{15}$ g s^{-1} for photon energies $E = 0.2E_{\rm cyc}$ (dotted orange lines), $0.4E_{\rm cyc}$ (solid red lines), $E_{\rm cyc}$ (dashed green lines) and $1.5E_{\rm cyc}$ (dot-dashed blue lines). The specific intensity $I_E(\theta)$ at the surface is assumed constant (parameter $b = 0$). Each curve is normalized to its maximum.

https://doi.org/10.3390/particles9020049

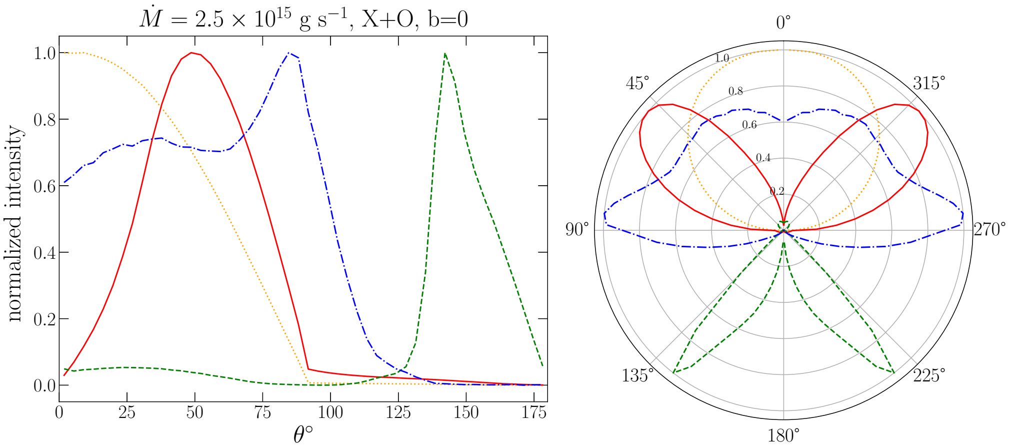

Figure 2. Same as in Figure 1 but for $\dot{M} = 2.5 \times 10^{15}$ g s^{-1}.

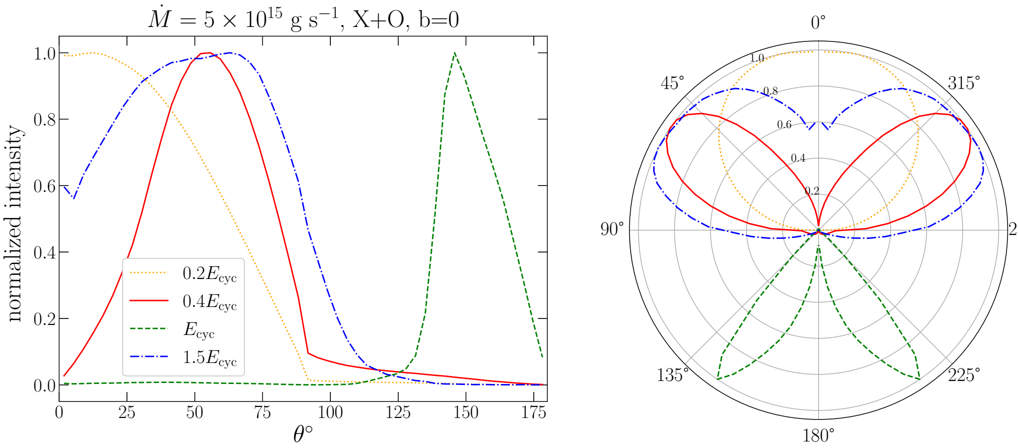

Figure 3. Same as in Figures 1 and 2 but for $\dot{M} = 5 \times 10^{15}$ g s^{-1}.

At the lowest energy $E = 0.2E_{\rm cyc}$, the optical thickness of the accretion channel is small; therefore, the corresponding (dotted) line is close to the initial surface beaming, which in this case was assumed isotropic (parameter b in Equation (3) is zero). At all other energies shown in the figure, including the rather low value $E = 0.4E_{\rm cyc}$, the beaming of the outgoing radiation is strongly anisotropic, unlike the initial one, which means that this pattern is formed due to the scattering in the accretion channel.

The fan-like pattern at $E = 0.4E_{\rm cyc}$ with strongly suppressed intensity around the normal to the surface appears due to the large optical depth for the photons propagating at small angles θ nearly along the cylindrical walls. The wall thickness $d_{\rm w}$ is much smaller than the cylinder height, so that the photons with large inclination angles escape easily.

For $E = E_{\rm cyc}$, the resonant Compton scattering diverts most photons back to the NS surface, which explains their concentration at $\theta > 90°$.

At a higher energy $E = 1.5E_{\rm cyc}$, multiple non-resonant scattering in the channel is substantial. At a low accretion rate $\dot{M} = 10^{15}$ g s^{-1} (Figure 1), the beaming pattern still resembles the pattern at the resonance, although a significant (albeit minor) fraction of photons escapes in the upper hemisphere $\theta < 90°$. With increasing $\dot{M}$ (Figures 2 and 3), the plasma density in the channel increases, the mean free path of a photon decreases, respectively, and the multiple scattering becomes more important. In these cases, we observe a broad angular distribution, slightly suppressed around the normal.

3.2. Influence of Boundary Conditions

Figures 4 and 5 show beaming of the outgoing radiation calculated assuming different boundary conditions. Figure 4 demonstrates the case where the radiation that enters the accretion channel from the NS surface is polarized. The left panel presents the case where the initial polarization is completely in the X-mode, and the right panel corresponds to the initial O-mode. Here, the accretion rate $\dot{M} = 2.5 \times 10^{15}$ g s^{-1} is assumed, as in Figure 2. We see that this change in boundary conditions affects the beaming noticeably, but not crucially. The beaming patterns at the different energies remain similar to those in Figure 2, although they are somewhat broader in the case where the initial polarization is ordinary compared with the opposite case of extraordinary initial polarization. The most significant difference occurs at the energy above the cyclotron resonance, where the broadening of the beaming pattern is significantly more anisotropic in the case of the initial X-mode.

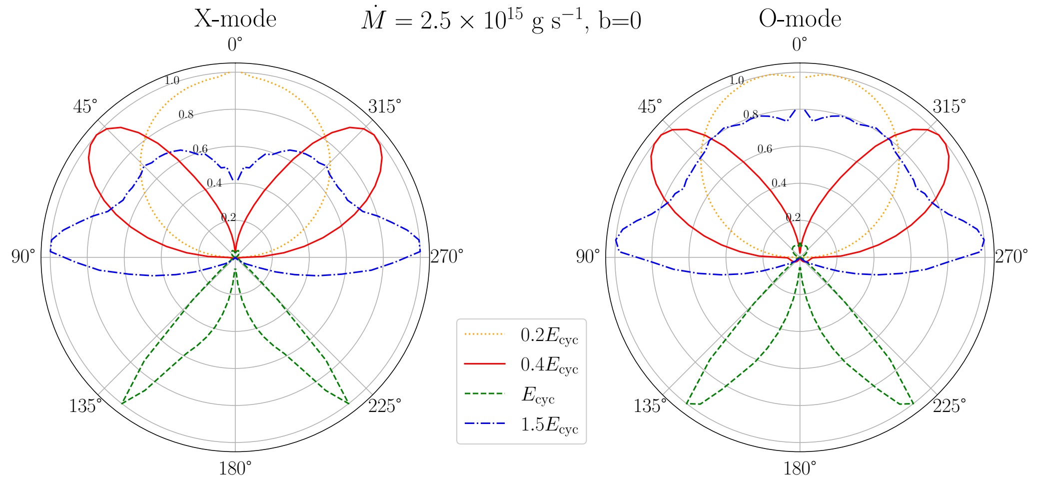

Figure 4. Polar diagram of outgoing radiation at $\dot{M} = 2.5 \times 10^{15}$ g s^{-1} (as in Figure 2) for separate polarizations of NS surface radiation: incoming X-mode (**left panel**) and incoming O-mode (**right panel**).

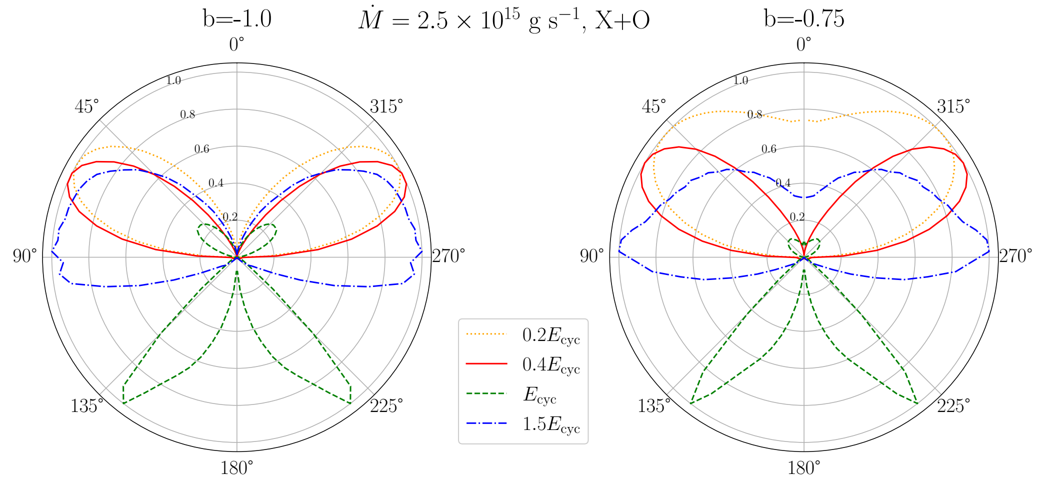

Figure 5. Polar diagram of beaming of outgoing radiation at $\dot{M} = 2.5 \times 10^{15}$ g s^{-1} for the unpolarized NS surface radiation, suppressed near the normal to the surface according to Equation (3) with parameter $b = -1$ (**left panel**) or $b = -0.75$ (**right panel**).

Figure 5 demonstrates beaming of the anisotropic radiation, coming into the bottom of the accretion channel from the NS surface according to Equation (3) with negative parameter b. This model corresponds to the initial beam pattern suppressed along the normal to the surface, as expected at very low accretion rates [21,42]. Here the incoming surface radiation is unpolarized, and the accretion rate is $\dot{M} = 2.5 \times 10^{15}$ g s^{-1}, as in Figure 2. The right panel presents the case of moderate initial anisotropy with $b = -0.75$ and the left panel shows the extreme case of $b = -1$. We see that the scattering in the accretion channel strongly modifies the beaming at not too low photon energies $E \geq 0.4E_{\rm cyc}$.

Still, the beaming pattern retains traces of the initial angular distribution. In particular, the radiation remains completely suppressed in the normal direction $\theta = 0$ in the case of $b = -1$.

3.3. Importance of Vacuum Polarization

In the previous paper [25], we simulated the radiation outgoing from the accretion channels of subcritical XRPs, taking into account the birefringence of strongly magnetized plasma, but neglecting the quantum-electrodynamical effect of vacuum polarization [31]. Recently, Sokolova-Lapa et al. [43] argued that this effect should be important for the formation of XRP spectra. Our new simulations fully take the vacuum polarization into account following the formalism of Ref. [34] (full details of our treatment are given in Ref. [26]). We show that the vacuum polarization effect is important not only for the spectra, but also for the beaming. It can be seen from a comparison of Figure 4 with Figure 6, the latter being different from the former one by neglecting the vacuum polarization effects. The comparison reveals pronounced differences in the beaming patterns. A more complex beaming is formed if the vacuum polarization is neglected, in which case the normal mode polarization ellipses are less elongated. The sharpest difference is observed in the case where the NS surface radiation is polarized in the O-mode (compare the right panels of Figures 4 and 6).

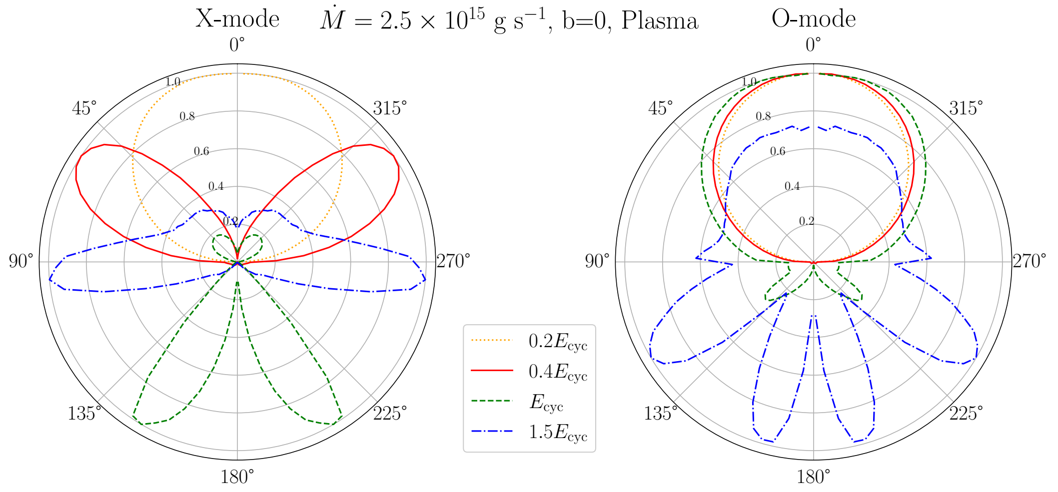

Figure 6. Same as in Figure 4, but in the "plasma approximation" where the vacuum polarization effects are neglected.

3.4. Polarization-Resolved Beaming

In Section 3.2, we considered the influence of polarization of the *incoming* radiation on the beaming of the outgoing radiation, summed over its polarization states. Let us now consider the beaming patterns separately for each of the two outgoing normal modes. Figure 7 shows the results for the case of $\dot{M} = 2.5 \times 10^{15}$ g s^{-1}, to be compared with Figure 2. We can notice a moderate difference in the beaming of the two modes at $E = 0.4E_{\rm cyc}$ and a significant difference at the higher energies $E \geq E_{\rm cyc}$, despite the incoming radiation was assumed unpolarized. This difference shows that the scattering in the accretion channel substantially affects the formation of the polarization of the XRP radiation (a more extensive study and discussion of the effects of the in-channel scattering on the polarization is given in Ref. [26]).

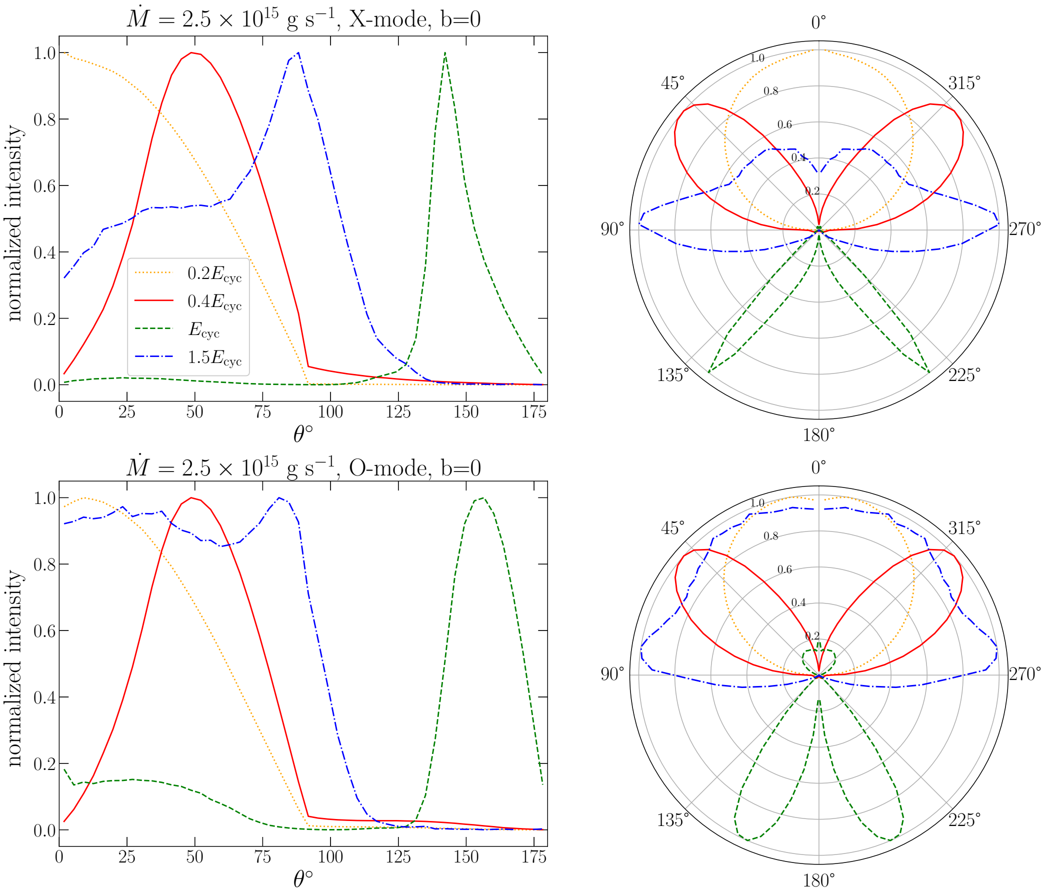

Figure 7. Same as in Figure 2, but separately for the outgoing X-mode (**upper panels**) and O-mode (**lower panels**).

3.5. Beaming as a Function of Photon Energy and Direction

In Figure 8, the intensity of radiation, normalized to its maximum as a function of θ at each E, is coded with color and shown in the θ–E plane. The bright yellow color corresponds to the maximum of intensity, and the dark violet to its minimum. The incoming radiation was assumed unpolarized and isotropic. This figure clarifies the origin of the differences between beaming patterns at different energies observed in Figures 1–3 and 7. The values of these energies are marked by the horizontal lines.

The upper panels in Figure 8 present the maps for the total intensity at two different accretion rates, and the lower panels present them separately for the X- and O-modes at an intermediate mass accretion rate. We see that there are two strips of clear maxima at different energies with a minimum in between, which drift from lower to higher E with increasing θ. At some energies, both strips can be crossed by corresponding horizontal lines, giving a complex beaming pattern like the dot-dashed line on the right panel of Figure 6. In addition, there is a local maximum at a nearly constant energy close to $E = E_{\rm cyc}$, which is more clearly seen in the upper-left and lower-right panels of Figure 8.

The wide dark valleys between the pairs of brighter strips, directed toward higher energies at larger angles θ, map phase regions in which the scattering optical thickness becomes greater than one. Thus scattering processes effectively remove the original photons from the phase region of the directions and energies corresponding to the dark valleys, which leads to the angular dependencies shown in Figures 1–3 and 7. These angular dependencies can be easily traced at each photon energy E by following the corresponding horizontal lines in Figure 8.

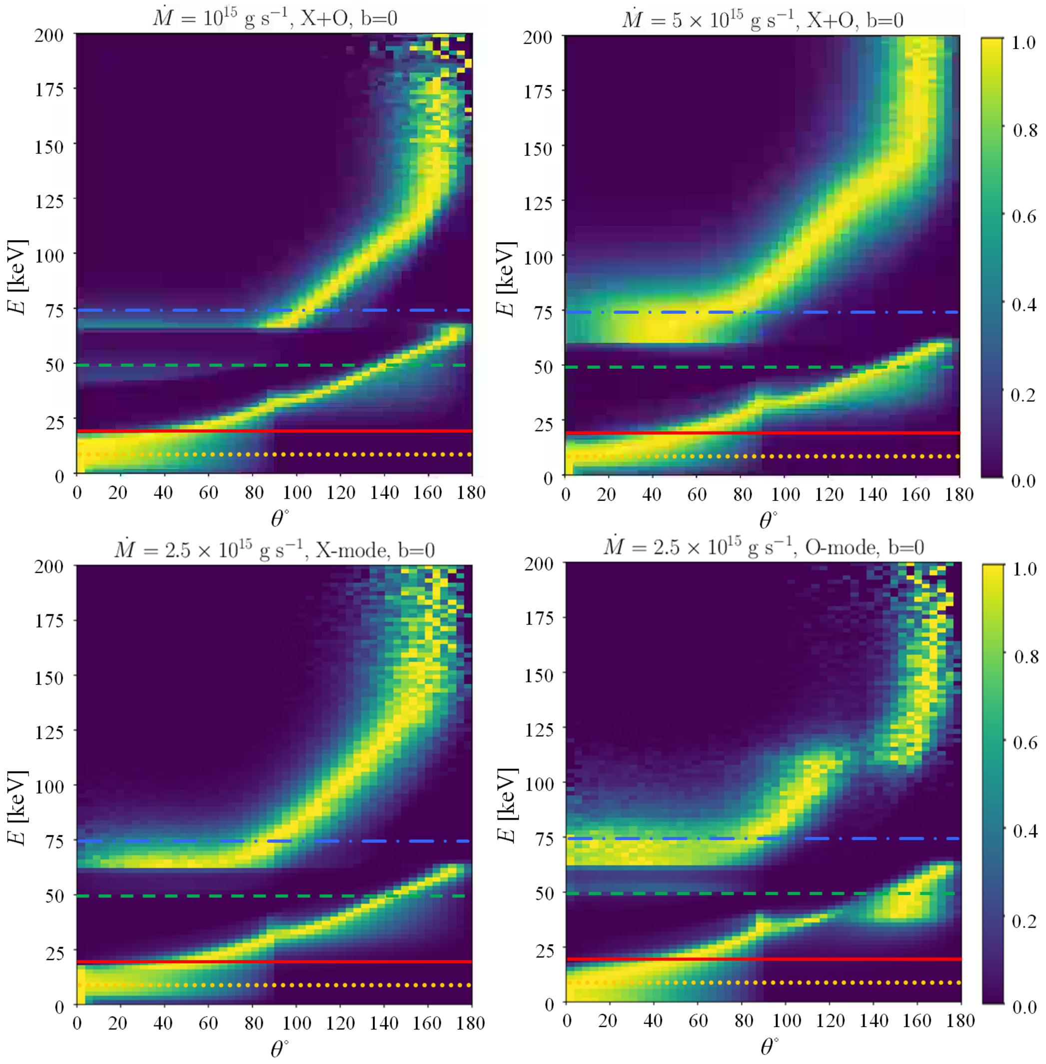

Figure 8. Color maps of the normalized intensity of outgoing radiation as functions of the angle to the NS surface normal θ (the horizontal axis, in degrees) and photon energy E (the vertical axis, in keV). **Upper panels**: total intensity for both normal modes for accretion rates $\dot{M} = 10^{15}$ g s^{-1} (**left panel**) and $\dot{M} = 5 \times 10^{15}$ g s^{-1} (**right panel**). **Lower panels**: the outgoing radiation polarized in the X-mode (**left panel**) and the O-mode (**right panel**) at the intermediate mass accretion rate $\dot{M} = 2.5 \times 10^{15}$ g s^{-1}. The horizontal lines are drawn at the energies for which the curves of the same types are plotted in the other figures.

3.6. Light Curves

The beaming patterns presented above determine the light curves of spectral flux and polarization of an XRP. Below, we present examples of such light curves, calculated in several approximations. First, we neglect the effects specific to NS rotation: shape flattening, general-relativistic frame dragging, Doppler boosting, and relativistic aberration [44–46]. This is a good approximation for the typical (not millisecond) X-ray pulsars. Second, we neglect the size of the emission region compared with the NS radius. Third, we assume that the X-ray photons that have escaped from this region propagate in the empty space. Then, each photon trajectory is a flat curve, which is accurately described by the analytical approximation of Poutanen [47], which gives the angle θ between the wave vector $\boldsymbol{k}$ and normal $\boldsymbol{n}$ to the NS surface in terms of elementary functions of the angle ψ between $\boldsymbol{n}$ and the direction to a distant observer.

For an infinitely narrow bundle of light rays with transverse cross section $\mathrm{d}S_\perp$ that reach a distant observer, the observed spectral flux density equals $\mathrm{d}F_E^\infty = I_E^\infty \mathrm{d}\Omega$, where I_E^∞ is the observed specific intensity and $\mathrm{d}\Omega$ is the solid angle that the element $\mathrm{d}S_\perp$ occupies in the observer's sky. Since the ratio I_E/E^3 is invariant (see, e.g., Section 22.6 in Ref. [48]) and the photon energy at infinity is decreased by the redshift factor $(1+z_\mathrm{g})^{-1}$, the specific intensity in the local reference frame at the NS surface is $I_E = I_E^\infty\,(1+z_\mathrm{g})^3$. On the other hand, $\mathrm{d}\Omega = \mathcal{D}\mathrm{d}S_\perp/D^2$, where D is the distance and $\mathcal{D} = (1+z_\mathrm{g})^2\,\mathrm{d}\cos\theta/\mathrm{d}\cos\psi \approx 1$ is the lensing factor, which is also accurately represented as a function of ψ by the approximation of Poutanen [47]. Thus,

$$F_E^\infty(\psi) = \frac{\mathcal{D}(\psi)Q_E(\theta(\psi))}{D^2\,(1+z_\mathrm{g})^3}, \tag{4}$$

where $Q_E = \int_{S_\perp} I_E \mathrm{d}S_\perp$ is the radiant intensity at the polar angle θ in the local reference frame. Since the backward radiation is intercepted by the NS surface, we set $F_E^\infty(\psi) = 0$ whenever $\theta(\psi) \geq 90^\circ$.

Since we neglect the size and geometry of the emitting zone, the angle ψ coincides with the angle between the magnetic axis of the star and the line of sight. Let α and ζ be the angles that the spin axis makes with the magnetic axis and with the line of sight, respectively. Then the light curve from a single accretion channel is given by Equation (4) with

$$\cos\psi = \sin\zeta\sin\alpha\cos(\phi-\phi_0) + \cos\zeta\cos\alpha, \tag{5}$$

where ϕ is the rotational phase and ϕ_0 is an arbitrary constant phase shift. To add an identical antipodal emitting area, one can use Equation (4) with ψ replaced by $\psi+\pi$.

Figure 9 shows examples of light curves for the intensity and polarization degree. To produce them, we have applied Equations (4) and (5) to the beaming of radiant intensities of the X- and O-modes, $Q_E = Q_E^\mathrm{X}(\theta)$ and $Q_E = Q_E^\mathrm{O}(\theta)$, respectively, shown in Figure 7. As stated above, we replace the real distribution of the outgoing photons over the surface of the accretion channel by a point source. This model is relevant within the scope of the present paper because it elucidates the clean effect of the beaming pattern, which is the main focus of study here, separated from such subtle factors as complex geometry of the emission zone. It is expected to be acceptable for the subcritical X-ray pulsars, because their emission zones have both the radii R_c and heights H much smaller than R_NS [41]. We have put $\phi_0 = 0$ in Equation (5), which means that the viewing angle of the primary emission zone is minimal at $\phi = 0$. The calculations have been done at four values of the emitted photon energy $E = 10$ keV, 20 keV, 50 keV and 75 keV, the same as in Figures 1–7, which correspond to the observed photon energies $E^\infty = E/(1+z_\mathrm{g}) = 8.1$ keV, 16.2 keV, 40.5 keV and 60.7 keV. The light curves produced by a single emission zone are shown by the thin lines, and the thick lines are given by the model of two symmetrical antipodal hot spots.

The light curves for the intensity present the sum of the flux densities F_E^∞ for the X- and O-modes, which we denote respectively $F_E^\mathrm{X}(\phi)$ and $F_E^\mathrm{O}(\phi)$, calculated as functions of the rotation phase $(\phi/2\pi)$ and normalized to the mean value according to the formula

$$f_E(\phi) = \frac{F_E^\mathrm{X}(\phi) + F_E^\mathrm{O}(\phi)}{\int_0^{2\pi}\left[F_E^\mathrm{X}(\phi') + F_E^\mathrm{O}(\phi')\right]\mathrm{d}\phi'/2\pi}. \tag{6}$$

We see that there can be a large variety of shapes of the light curves, depending on the geometry settings and photon energy. It is easy to trace the origin of the properties (minima and maxima) of each light curve in the beaming pattern of the corresponding total radiant intensity $Q_E^\mathrm{X}(\theta) + Q_E^\mathrm{O}(\theta)$ near the NS surface, shown in Figure 2. In particular, for the lowest photon energy $E = 0.2E_\mathrm{cyc}$ (the dotted orange curve) f_E in Figure 9 has a maximum at $\phi = 0$, which corresponds to the maximum of the initial radiant intensity Q_E at $\theta = 0$, while for $E = 0.4E_\mathrm{cyc}$ (the solid red line) f_E has a minimum at $\phi = 0$ and a maximum at an intermediate phase, which correspond to the fan-type beaming pattern of Q_E at this E value.

In Figure 10, in contrast, the low-energy curve has a minimum at $\phi = 0$, corresponding to the minimum of the initial intensity at $\theta = 0$. In the extreme case of $\alpha = \zeta = 90°$, each light curve in the model with two opposite hot spots displays an apparent period equal to one half of the true rotation period, because of the alternating appearance of the two identical antipodal emission zones. The jumps (vertical segments of the light curves) in this model occur at the phase values, where both hot spots become visible simultaneously due to the light bending (the jumps up) where one of them becomes invisible behind the horizon (the jumps down). These jumps would be smeared over a narrow but finite phase interval were the finite size of each emission zone taken into account. The light curves produced by a single spot trace the beaming pattern more directly, while in the two-spot model the secondary maximum on the light curve, produced by the second spot at an intermediate phase, may override the primary minimum related to the beaming—compare, for instance, the thick and thin red lines in the case of $(\alpha, \zeta) = (30°, 60°)$ in both Figures 9 and 10.

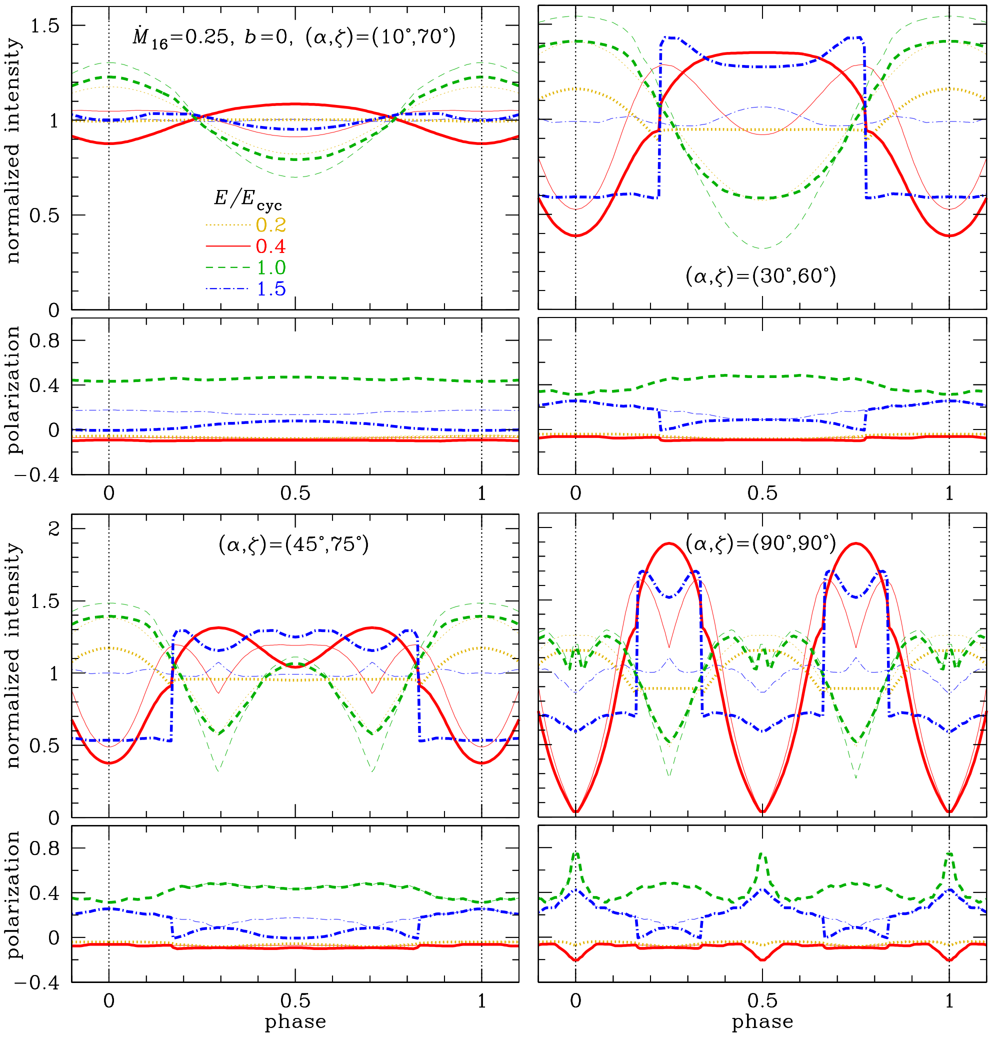

Figure 9. Light curves for the intensity and polarization degree, corresponding to the beaming patterns shown in Figure 7 ($M = 1.4\,M_\odot$, $R_{\rm NS} = 12$ km, $\dot{M} = 2.5 \times 10^{15}$ g s^{-1}, input beaming parameter $b = 0$) for different combinations of the angles α and ζ that the spin axis makes with the magnetic axis and the line of sight. Different line types correspond to different energies of outgoing photons in the local NS reference frame. The thick and thin lines of the same type show the models with two antipodal emission spots and with a single spot, respectively.

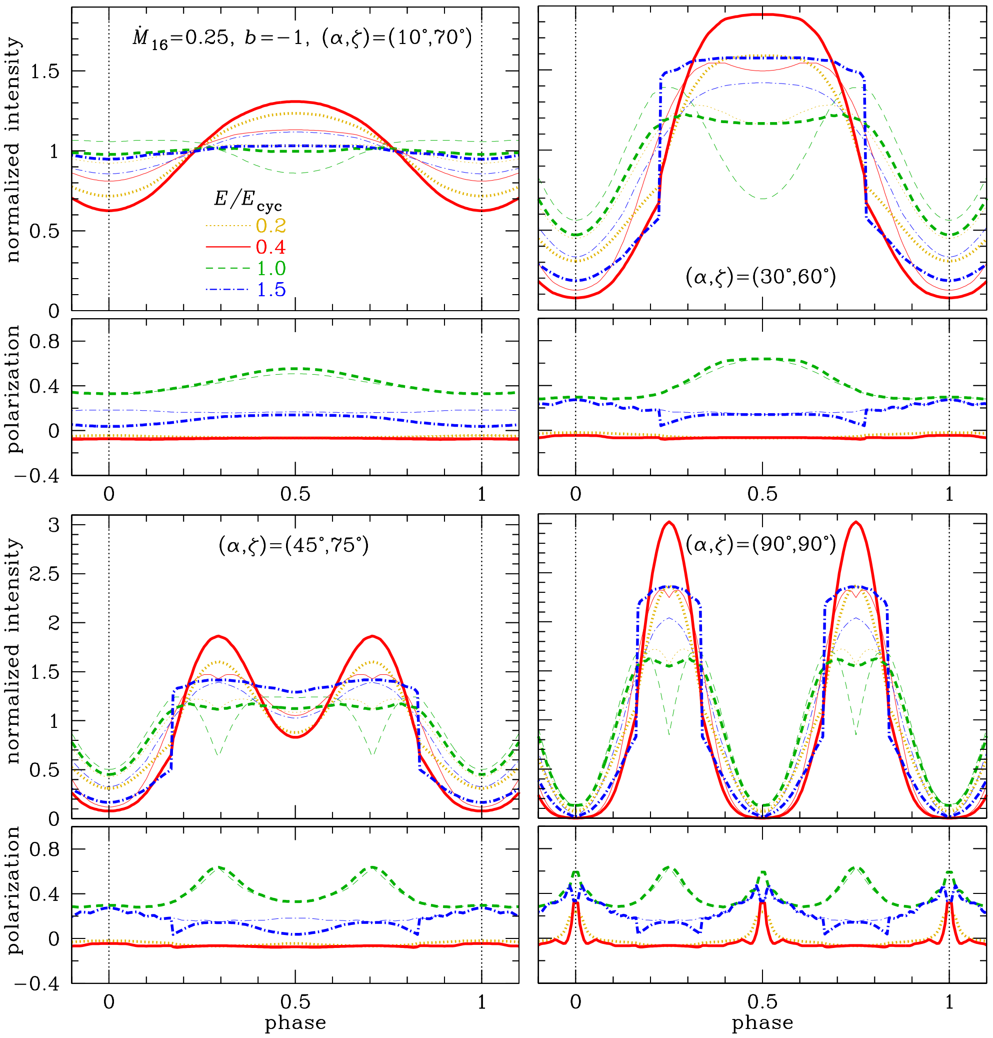

Figure 10. Same as in Figure 9 but for the fan-like input beaming with parameter $b = -1$.

The polarization curves are calculated according to

$$P_{\rm O-X}(\phi) = \frac{F_E^{\rm O}(\phi) - F_E^{\rm X}(\phi)}{F_E^{\rm O}(\phi) + F_E^{\rm X}(\phi)}. \tag{7}$$

Taking into account that the linear polarization degree equals

$$P_L = \frac{I_{\rm O} - I_{\rm X}}{I_{\rm O} + I_{\rm X}} p_1, \tag{8}$$

where $I_{\rm O}$ is the O-mode intensity, $I_{\rm X}$ is the X-mode intensity and p_1 is the linear polarization degree of a single normal mode, we see that $P_{\rm O-X}$ is close to the observed P_L, provided that $p_1 \approx 1$, which is indeed the case if the normal mode ellipticity is dominated by the vacuum polarization. Although the initial radiation from the NS surface was taken unpolarized in the shown examples, the observed polarization degree is significant at some phases for sufficiently high photon energies and especially at $E = E_{\rm cyc}$, which highlights the effect of the resonant Compton scattering in the accretion channel at such E values.

3.7. Connection to Observations

Although we do not perform a direct calculation of pulse profiles or the pulsed fraction (PF) as a function of photon energy, our results allow for a qualitative comparison with observational data.

Observational studies of accreting X-ray pulsars indicate that both the pulse profile and the pulsed fraction depend on photon energy. In particular, a local minimum or, more generally, a distinct feature in PF(E) near the cyclotron resonance energy has been reported for a number of subcritical sources (see, e.g., [49,50]). Such behavior is observed, for instance, in sources like V 0332+53, 4U 0115+63 and Her X-1. Our simulations show a qualitatively similar behavior in most (although not all) of the considered geometries. In the vicinity of $E \sim E_{\rm cyc}$, resonant Compton scattering redistributes photons over angles, leading to a less anisotropic emission pattern. As a result, the light curve amplitude decreases, which implies a reduction in the pulsed fraction. This effect is evident from Figures 9 and 10, where the modulation amplitude of the simulated light curves is smaller at the cyclotron energy $E_{\rm cyc}$ than at the neighboring energies ($0.4\,E_{\rm cyc}$ and $1.5\,E_{\rm cyc}$) in three of the four combinations of angles (α, ζ) for the model of two symmetric hot spots, if an isotropic surface radiation is assumed (i.e., the anisotropy parameter $b = 0$, the thick curves in Figure 9), and for all considered combinations of (α, ζ) and both one- and two-spot models, if the surface radiation is assumed to be suppressed near the normal ($b = -1$, Figure 10).

The fact that the cyclotron suppression of the pulsed fraction is present not for all parameter sets in our calculations is consistent with observational results showing that the behavior of PF(E) near the cyclotron energy is not universal. A quantitative analysis of the simulated PF(E) and its detailed comparison with observations is beyond the scope of the present work.

4. Conclusions

We have studied beaming patterns and light curves of subcritical XRPs. For typical parameters of such XRPs, we have numerically solved the radiation hydrodynamics equations for the structure of the accretion channel and performed Monte Carlo simulations of radiative transfer in this channel. The resulting beaming patterns for the outgoing radiation at photon energies $E \geq 0.4E_{\rm cyc}$ differ drastically from the beaming pattern of the radiation injected into the accretion channel from the NS surface. In particular, the beaming pattern is strongly anisotropic and polarized even for an isotropic unpolarized surface emission. There is a moderate dependence of the resulting beaming pattern on the boundary conditions (the polarization and beaming of the incoming surface radiation) at $E \geq 0.4E_{\rm cyc}$ and a stronger dependence on the accretion rate at $E > E_{\rm cyc}$. We have demonstrated that the account of the vacuum polarization is necessary for a correct simulation of the beaming: were it neglected, the beaming pattern would be very different.

The calculated beaming patterns have been implemented in modeling light curves of the subcritical XRPs. Manifestations of properties of the beaming pattern have been demonstrated on examples for the dependencies of the observable flux density and polarization degree on the rotational phase of an XRP.

Our results also provide a qualitative link to observational studies of energy-dependent pulse profiles. The angular redistribution of radiation caused by resonant Compton scattering near $E \sim E_{\rm cyc}$ reduces the anisotropy of the emerging emission and, consequently, the modulation amplitude of the light curves. This behavior is consistent with observational indications that the pulsed fraction may exhibit a local decrease or a distinct feature near the cyclotron resonance energy in some subcritical X-ray pulsars [50].

Author Contributions: Conceptualization, methodology, and investigation, I.D.M., A.Y.P., A.D.K. and A.A.M.; software, I.D.M.; writing—original draft preparation, A.Y.P.; writing—review and editing, I.D.M., A.Y.P., A.D.K. and A.A.M.; visualization, I.D.M. and A.Y.P. All authors have read and agreed to the published version of the manuscript.

Funding: The research of I.M. was supported by the Foundation for the Advancement of Theoretical Physics and Mathematics "BASIS". The research of A.P. was supported by the Ministry of Science and Higher Education of the Russian Federation (agreement no. 075-15-2024-647).

Data Availability Statement: The original contributions presented in this study are included in the article. Further inquiries can be directed to the authors.

Acknowledgments: This research was supported by the International Space Science Institute (ISSI) in Bern, through International Team project 25-657 "Polarimetric Insights into Extreme Magnetism". I.M. and A.P. thank for hospitality the organizers of the international conference "The Modern Physics of Compact Stars and Relativistic Gravity 2025" in Yerevan, which promoted the present work.

Conflicts of Interest: The authors declare no conflicts of interest.

References

1. Mushtukov, A.; Tsygankov, S., Accreting strongly magnetised neutron stars: X-ray pulsars. In *Handbook of X-Ray and Gamma-Ray Astrophysics*; Bambi, C.; Santangelo, A., Eds.; Springer: Singapore, 2024; pp. 4105–4136. https://doi.org/10.1007/978-981-19-6960-7.
2. Yang, J.; Laycock, S.G.T.; Christodoulou, D.M.; Fingerman, S.; Coe, M.J.; Drake, J.J. A comprehensive library of X-ray pulsars in the Small Magellanic Cloud: Time evolution of their luminosities and spin periods. *Astrophys. J.* **2017**, *839*, 119. https://doi.org/10.3847/1538-4357/aa6898.
3. Bachetti, M.; Harrison, F.A.; Walton, D.J.; Grefenstette, B.W.; Chakrabarty, D.; Fürst, F.; Barret, D.; Beloborodov, A.; Boggs, S.E.; Christensen, F.E.; et al. An ultraluminous X-ray source powered by an accreting neutron star. *Nature* **2014**, *514*, 202–204. https://doi.org/10.1038/nature13791.
4. Israel, G.L.; Belfiore, A.; Stella, L.; Esposito, P.; Casella, P.; De Luca, A.; Marelli, M.; Papitto, A.; Perri, M.; Puccetti, S.; et al. An accreting pulsar with extreme properties drives an ultraluminous X-ray source in NGC 5907. *Science* **2017**, *355*, 817–819, https://doi.org/10.1126/science.aai8635.
5. King, A.; Lasota, J.P. ULXs: Neutron stars versus black holes. *Mon. Not. R. Astron. Soc.* **2016**, *458*, L10–L13. https://doi.org/10.1093/mnrasl/slw011.
6. King, A.; Lasota, J.P.; Kluźniak, W. Pulsing ULXs: tip of the iceberg? *Mon. Not. R. Astron. Soc.* **2017**, *468*, L59–L62. https://doi.org/10.1093/mnrasl/slx020.
7. Lasota, J.P.; King, A. Ultraluminous X-ray sources are beamed. *Mon. Not. R. Astron. Soc.* **2023**, *526*, 2506–2509. https://doi.org/10.1093/mnras/stad2926.
8. Mushtukov, A.A.; Portegies Zwart, S. Bright X-ray pulsars: how outflows influence beaming, pulsations and pulse phase lags. *Mon. Not. R. Astron. Soc.* **2023**, *518*, 5457–5464. https://doi.org/10.1093/mnras/stac3431.
9. Tsygankov, S.S.; Mushtukov, A.A.; Suleimanov, V.F.; Doroshenko, V.; Abolmasov, P.K.; Lutovinov, A.A.; Poutanen, J. Stable accretion from a cold disc in highly magnetized neutron stars. *Astron. Astrophys.* **2017**, *608*, A17. https://doi.org/10.1051/0004-6361/201630248.
10. Tsygankov, S.S.; Doroshenko, V.; Mushtukov, A.A.; Lutovinov, A.A.; Poutanen, J. Study of the X-ray pulsar IGR J19294+1816 with NuSTAR: Detection of cyclotron line and transition to accretion from the cold disk. *Astron. Astrophys.* **2019**, *621*, A134. https://doi.org/10.1051/0004-6361/201833786.
11. Illarionov, A.F.; Sunyaev, R.A. Why the Number of Galactic X-ray Stars Is so Small? *Astron. Astrophys.* **1975**, *39*, 185.
12. Staubert, R.; Trümper, J.; Kendziorra, E.; Klochkov, D.; Postnov, K.; Kretschmar, P.; Pottschmidt, K.; Haberl, F.; Rothschild, R.E.; Santangelo, A.; et al. Cyclotron lines in highly magnetized neutron stars. *Astron. Astrophys.* **2019**, *622*, A61. https://doi.org/10.1051/0004-6361/201834479.
13. Weisskopf, M.C.; Soffitta, P.; Baldini, L.; Ramsey, B.D.; O'Dell, S.L.; Romani, R.W.; Matt, G.; Deininger, W.D.; Baumgartner, W.H.; Bellazzini, R.; et al. The Imaging X-Ray Polarimetry Explorer (IXPE): Pre-Launch. *J. Astron. Telesc. Instruments Syst.* **2022**, *8*, 026002. https://doi.org/10.1117/1.JATIS.8.2.026002.
14. Heyl, J. Remembering Yury N. Gnedin at the dawn of X-ray polarimetry: Predictions of IXPE observations of neutron stars. *Universe* **2022**, *8*, 84. https://doi.org/10.3390/universe8020084.
15. Doroshenko, V.; Poutanen, J.; Tsygankov, S.S.; Suleimanov, V.F.; Bachetti, M.; Caiazzo, I.; Costa, E.; Di Marco, A.; Heyl, J.; La Monaca, F.; et al. Determination of X-ray pulsar geometry with IXPE polarimetry. *Nat. Astron.* **2022**, *6*, 1433–1443. https://doi.org/10.1038/s41550-022-01799-5.
16. Mitra, A. Maximum Accretion Efficiency in General Theory of Relativity. *arXiv* **1998**. https://doi.org/10.48550/arXiv.astro-ph/9811402.

17. Meisel, Z.; Deibel, A.; Keek, L.; Shternin, P.; Elfritz, J. Nuclear physics of the outer layers of accreting neutron stars. *J. Phys. G Nucl. Phys.* **2018**, *45*, 093001. https://doi.org/10.1088/1361-6471/aad171.
18. Davidson, K. Accretion at a magnetic pole of a neutron star. *Nat. Phys. Sci.* **1973**, *246*, 1–4. https://doi.org/10.1038/physci246001a0.
19. Basko, M.M.; Sunyaev, R.A. The limiting luminosity of accreting neutron stars with magnetic fields. *Mon. Not. R. Astron. Soc.* **1976**, *175*, 395–417. https://doi.org/10.1093/mnras/175.2.395.
20. Zel'dovich, Y.B.; Shakura, N.I. X-Ray Emission Accompanying the Accretion of Gas by a Neutron Star. *Sov. Astron.* **1969**, *13*, 175.
21. Sokolova-Lapa, E.; Gornostaev, M.; Wilms, J.; Ballhausen, R.; Falkner, S.; Postnov, K.; Thalhammer, P.; Fürst, F.; García, J.A.; Shakura, N.; et al. X-ray emission from magnetized neutron star atmospheres at low mass-accretion rates. I. Phase-averaged spectrum. *Astron. Astrophys.* **2021**, *651*, A12. https://doi.org/10.1051/0004-6361/202040228.
22. Shapiro, S.L.; Salpeter, E.E. Accretion onto neutron stars under adiabatic shock conditions. *Astrophys. J.* **1975**, *198*, 671–682. https://doi.org/10.1086/153645.
23. Langer, S.H.; Rappaport, S. Low-luminosity accretion onto magnetized neutron stars. *Astrophys. J.* **1982**, *257*, 733–751. https://doi.org/10.1086/160028.
24. Bykov, A.M.; Krassilchtchikov, A.M. Dynamics of the flows accreting onto a magnetized neutron star. *Astron. Lett.* **2004**, *30*, 309–318. https://doi.org/10.1134/1.1738153.
25. Markozov, I.D.; Kaminker, A.D.; Potekhin, A.Y. Hydrodynamical simulation of the structure of the X-ray pulsar accretion channel: Accounting for resonant scattering. *Astron. Lett.* **2023**, *49*, 583–590. https://doi.org/10.1134/S1063773723100031.
26. Markozov, I.D.; Potekhin, A.Y.; Kaminker, A.D.; Mushtukov, A.A. The influence of vacuum polarization on plasma braking and radiation transfer in subcritical X-ray pulsars. *Mon. Not. R. Astron. Soc.*, *to be published*.
27. Ginzburg, V.L. *The Propagation of Electromagnetic Waves in Plasmas*, 2nd ed.; Freeman and Co.: New York, NY, USA, 1970.
28. Gnedin, Y.N.; Pavlov, G.G. The transfer equations for normal waves and radiation polarization in an anisotropic medium. *Sov. Phys. JETP* **1974**, *38*, 903–908.
29. Novick, R.; Weisskopf, M.C.; Angel, J.R.P.; Sutherland, P.G. The effect of vacuum birefringence on the polarization of X-ray binaries and pulsars. *Astrophys. J.* **1977**, *215*, L117–L120. https://doi.org/10.1086/182492.
30. Gnedin, Y.N.; Pavlov, G.G.; Shibanov, Y.A. The effect of vacuum birefringence in a magnetic field on the polarization and beaming of X-ray pulsars. *Sov. Astron. Lett.* **1978**, *4*, 117–119.
31. Pavlov, G.G.; Gnedin, Y.N. Vacuum polarization by a magnetic field and its astrophysical manifestations. *Sov. Sci. Rev. E Astrophys. Space Phys. Rev.* **1984**, *3*, 197.
32. Lai, D.; Ho, W.C.G. Resonant Conversion of Photon Modes Due to Vacuum Polarization in a Magnetized Plasma: Implications for X-Ray Emission from Magnetars. *Astrophys. J.* **2002**, *566*, 373–377. https://doi.org/10.1086/338074.
33. Ho, W.C.G.; Lai, D. Atmospheres and spectra of strongly magnetized neutron stars - II. The effect of vacuum polarization. *Mon. Not. R. Astron. Soc.* **2003**, *338*, 233–252. https://doi.org/10.1046/j.1365-8711.2003.06047.x.
34. Lai, D.; Ho, W.C.G. Transfer of Polarized Radiation in Strongly Magnetized Plasmas and Thermal Emission from Magnetars: Effect of Vacuum Polarization. *Astrophys. J.* **2003**, *588*, 962–974. https://doi.org/10.1086/374334.
35. van Adelsberg, M.; Lai, D. Atmosphere models of magnetized neutron stars: QED effects, radiation spectra and polarization signals. *Mon. Not. R. Astron. Soc.* **2006**, *373*, 1495–1522. https://doi.org/10.1111/j.1365-2966.2006.11098.x.
36. Mushtukov, A.A.; Markozov, I.D.; Suleimanov, V.F.; Nagirner, D.I.; Kaminker, A.D.; Potekhin, A.Y.; Portegies Zwart, S. Statistical features of multiple Compton scattering in a strong magnetic field. *Phys. Rev. D* **2022**, *105*, 103027. https://doi.org/10.1103/PhysRevD.105.103027.
37. Mészáros, P. *High-Energy Radiation from Magnetized Neutron Stars*; University of Chicago Press: Chicago, IL, USA, 1992.
38. Herold, H. Compton and Thomson scattering in strong magnetic fields. *Phys. Rev. D* **1979**, *19*, 2868–2875. https://doi.org/10.1103/PhysRevD.19.2868.
39. LeVeque, R.J. *Finite Volume Methods for Hyperbolic Problems*; Cambridge Texts in Applied Mathematics; Cambridge University Press: Cambridge, UK, 2002.
40. Colella, P.; Woodward, P.R. The Piecewise Parabolic Method (PPM) for Gas-Dynamical Simulations. *J. Comput. Phys.* **1984**, *54*, 174–201. https://doi.org/10.1016/0021-9991(84)90143-8.
41. Suleimanov, V.F.; Lipunova, G.V.; Shakura, N.I. The thickness of accretion α-disks: Theory and observations. *Astron. Rep.* **2007**, *51*, 549–562. https://doi.org/10.1134/S1063772907070049.
42. Mushtukov, A.A.; Suleimanov, V.F.; Tsygankov, S.S.; Portegies Zwart, S. Spectrum formation in X-ray pulsars at very low mass accretion rate: Monte Carlo approach. *Mon. Not. R. Astron. Soc.* **2021**, *503*, 5193–5203. https://doi.org/10.1093/mnras/stab811.
43. Sokolova-Lapa, E.; Stierhof, J.; Dauser, T.; Wilms, J. Vacuum polarization alters the spectra of accreting X-ray pulsars. *Astron. Astrophys.* **2023**, *674*, L2. https://doi.org/10.1051/0004-6361/202346265.
44. Stergioulas, N. Rotating stars in relativity. *Living Rev. Relativ.* **2003**, *6*, 3. https://doi.org/10.12942/lrr-2003-3.

45. Poutanen, J.; Beloborodov, A.M. Pulse profiles of millisecond pulsars and their Fourier amplitudes. *Mon. Not. R. Astron. Soc.* **2006**, *373*, 836–844. https://doi.org/10.1111/j.1365-2966.2006.11088.x.
46. Poutanen, J. Relativistic rotating vector model for X-ray millisecond pulsars. *Astron. Astrophys.* **2020**, *641*, A166. https://doi.org/10.1051/0004-6361/202038689.
47. Poutanen, J. Accurate analytic formula for light bending in Schwarzschild metric. *Astron. Astrophys.* **2020**, *640*, A24. https://doi.org/10.1051/0004-6361/202037471.
48. Misner, C.W.; Thorne, K.S.; Wheeler, J.A. *Gravitation*; Freeman and Co.: New York, NY, USA, 1973.
49. Lutovinov, A.A.; Tsygankov, S.S. Timing characteristics of the hard X-ray emission from bright X-ray pulsars based on INTEGRAL data. *Astron. Lett.* **2009**, *35*, 433–456. https://doi.org/10.1134/S1063773709070019.
50. Ferrigno, C.; D'Aì, A.; Ambrosi, E. Energy-resolved pulse profiles of accreting pulsars: Diagnostic tools for spectral features. *Astron. Astrophys.* **2023**, *677*, A103. https://doi.org/10.1051/0004-6361/202347062.

Disclaimer/Publisher's Note: The statements, opinions and data contained in all publications are solely those of the individual author(s) and contributor(s) and not of MDPI and/or the editor(s). MDPI and/or the editor(s) disclaim responsibility for any injury to people or property resulting from any ideas, methods, instructions or products referred to in the content.